Supporting Information

A facile strategy for synthesis of spinel ferrite nano-granules and its potential applications

Derang Cao[a], Lining Pan[a], Hao Li[b], Jianan Li[a], Xicheng Wang[b], Xiaohong Cheng[a], Zhenkun Wang[a], Jianbo Wang[a,b] and Qingfang Liu[a]†

[1]Key Laboratory for Magnetism and Magnetic Materials of the Ministry of Education, Lanzhou University, Lanzhou 730000, People's Republic of China

[2]Key Laboratory of Special Function Materials and Structure Design, Ministry of Education, Lanzhou University, Lanzhou 730000, People's Republic of China

Corresponding author: liuqf@lzu.edu.cn (Qingfang Liu)

Tel: +86-931-8914171, Fax: +86-931-8914160

Part I

Detailed various experimental conditions for synthesis of MFe_2O_4 nano-granules.

Part II

The results of obtained MFe_2O_4 nano-granules with different DMF concentration.

Part III

The results of obtained MFe_2O_4 nano-granules under different calcination temperatures.

Part IV

Summary of the suitable preparing parameters and synthesizing other MFe_2O_4 nano-granules.

Part V

The possibility of synthesizing magnetite γ-Fe_2O_3 nano-granules.

Part VI

The possibility of preparing MFe_2O_4 nano-granules doped with nonmetal elements.

Part I

Detailed various experimental conditions for synthesis of MFe_2O_4 nano-granules.

Experimental Section

I. A unified methodology is provided using a simple and convenient route to for assembling materials. Ferric nitrate (0.4 mol/L), and M nitrate (i.e. cobalt nitrate, nickel nitrate, and zinc nitrate) (0.2 mol/L) were dissolved in Dimethyl Formamide (DMF, 15 mL). For the binary ferrite, we add two different metal nitrate salts (e.g., for $NiZnFe_2O_4$ nano-granules, M nitrate (0.2 mol/L) nickel nitrate (0.1 mol/L) and zinc nitrate (0.1 mol/L)). The mixed solution was calcined for 2 hours at the certain temperature under the air with the heating rate of 1℃/min. The obtained products are MFe_2O_4 nano-granules. This is the total strategy of the method, and the brief schematic diagram of experimentation is shown in Figure S1. The detailed process of every experiment is shown as follows.

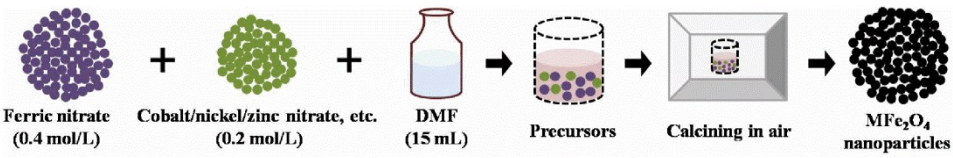

Figure S1. Schematic diagram of the simple experiment process.

II. MFe_2O_4 nano-granules with different DMF concentration were prepared at 650℃. The calcination time was 2 hours under the air, and the heating rate was 1℃/min. The concentration of DMF was regulated by adding distilled water, and the total volumes of DMF and water are still 15 mL. The obtained various DMF concentrations are 0% (pure distilled water), 13%, 33%, 53%, 67%, 87%, and 100% (pure DMF).

III. The experimental condition of MFe_2O_4 nano-granules under different calcination temperature (CT) was not changed. The heating temperature was established with 100℃, 200℃, 300℃, 400℃, 500℃, 600℃, 700℃, 800℃, and 900℃. The calcination time is still 2 hours under the air, and the heating rate was 1℃/min. The

total volumes of pure DMF are 15 mL.

IV. MFe_2O_4 ($ZnFe_2O_4$, $CuFe_2O_4$, $MnFe_2O_4$) nano-granules were obtained at 680℃for 2 hours under the air, and the heating rate was 1℃/min. The concentration of chemicals keeps the same, and the total volumes of pure DMF are 15 mL. Just replace M nitrate to zinc nitrate, copper nitrate, or manganese nitrate.

V. For preparing γ-Fe_2O_3, only ferric nitrate (0.6 mol/L) was dissolved in DMF (15 mL). The calcination temperature (CT) was 100℃, 150℃, 200℃, 250℃, 300℃, 350℃, and 400℃ for 2 hours under the air, and the heating rate was 1℃/min.

VI. The modified MFe_2O_4 nano-granules, i.e., nonmetal-doped $CoFe_2O_4$, were obtained at 680℃for 2 hour under the air, and the heating rate was 1℃/min. The precursor of S-doped $CoFe_2O_4$ was component with Ferric nitrate (0.4 mol/L), cobalt nitrate (0.2 mol/L), and different concentration thiourea (0 mol/L, 0.05 mol/L, 0.1 mol/L, 0.18 mol/L, 0.3 mol/L, and 0.5 mol/L) in DMF. The precursor of C-doped $CoFe_2O_4$ was component with Ferric nitrate (0.4 mol/L), cobalt nitrate (0.2 mol/L), and citric acid (0 mol/L, 0.03 mol/L, 0.08 mol/L, 0.15 mol/L, 0.3 mol/L, and 0.5 mol/L) in DMF.

Characterizations

The crystal structure of samples was measured by X-ray diffraction (XRD, PANalytical X'Pert) equipped with Cu-Kα radiation (λ=1.5406 Å). The morphology of all samples was observed by using field emission scanning electron microscopy (FESEM, Hitachi S-4800) equipped with an energy-dispersive spectrometer (EDS) X-ray spectrometer and transmission electron microscopy (HRTEM, Tecnai G^2 F30, FEI) equipped a high angle annular dark field detector (HAADF) in the scanning transmission electron microscopy (STEM) system. The X-ray photoelectron spectroscopy (XPS, PHI-5702, Physical Electronics) was performed using a monochromatic Al-Kα irradiation and a charge neutralizer. All binding energies were referred to the C1s peak at 284.6 eV of the surface adventitious carbon. The magnetic properties of the samples were measured by a vibrating sample magnetometer (VSM, Lakeshore 7304).

Part II

The results of obtained MFe_2O_4 nano-granules with different DMF concentration.

Figure S2 shows XRD spectra of obtained $NiFe_2O_4$, $CoFe_2O_4$, and $NiZnFe_2O_4$ nano-granules with different DMF concentration. The results reveal that the impurity α-Fe_2O_3 (JCPDS 80-2377) phases are generated in MFe_2O_4 nano-granules. In detail, α-Fe_2O_3 phase increases with the improvement of DMF concentration (0%~33%), but when the DMF concentration continues increasing, the impurity phase (α-Fe_2O_3) decreases gradually, and then nearly disappears. Comparing with the results of $CoFe_2O_4$ nano-granules (Figure S2b-c), particularly, α-Fe_2O_3 phase can be observed at the high DMF concentration (>87%) in $NiFe_2O_4$ and $NiZnFe_2O_4$, this is due to the higher crystalline temperature of $NiFe_2O_4$ and $NiZnFe_2O_4$ than that of $CoFe_2O_4$. The below results of different calcination temperatures can prove this view.

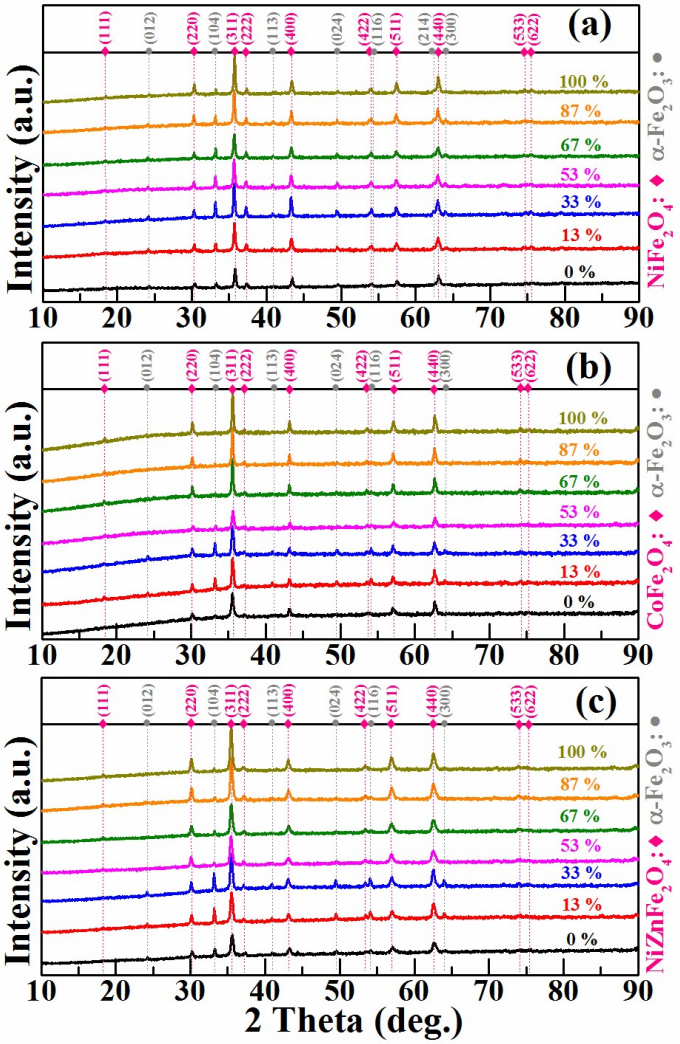

Figure S2. XRD patterns of $NiFe_2O_4$ (a), $CoFe_2O_4$ (b), and $NiZnFe_2O_4$ (c) nano-granules with different DMF concentration.

SEM pictures of $NiFe_2O_4$, $CoFe_2O_4$, and $NiZnFe_2O_4$ nano-granules with different DMF concentration are presented in Figure S3, S4, and S5, respectively. The results indicate the morphologies of all samples change gradually from bulk and dispersive particles to the compact and smooth nano-granules with the improvement of DMF concentration (Figure S3, S4, and S5, a-d). As the DMF concentration is increased (Figure S3, S4, and S5, e-g), large amounts of uniform nano-granules are observed. The detailed formation process is discussed below. The nano-granules formed in distilled water (DMF concentration is 0%) are irregular and littery, and reunite bulk together (Figure S3-S5a). But DMF coated nano-granules are smooth and near-sphere. When the samples are calcined at low DMF concentration (13~33%), the nano-granules are composed with irregular and littery bulk particles (Which are formed by distilled water) and smooth and flat granules (Which are formed by DMF), the results can be seen clearly in Figure S3-S5 (b-c). Afterwards, the granules become more uniform and smooth with the improvement of DMF concentration (53~67%), which are shown in Figure S3-S5 (d-e). Finally, DMF concentration is close to saturation (87~100%), large area and smooth nano-granules with uniform size are achieved, especially in the pure DMF concentration (100%).

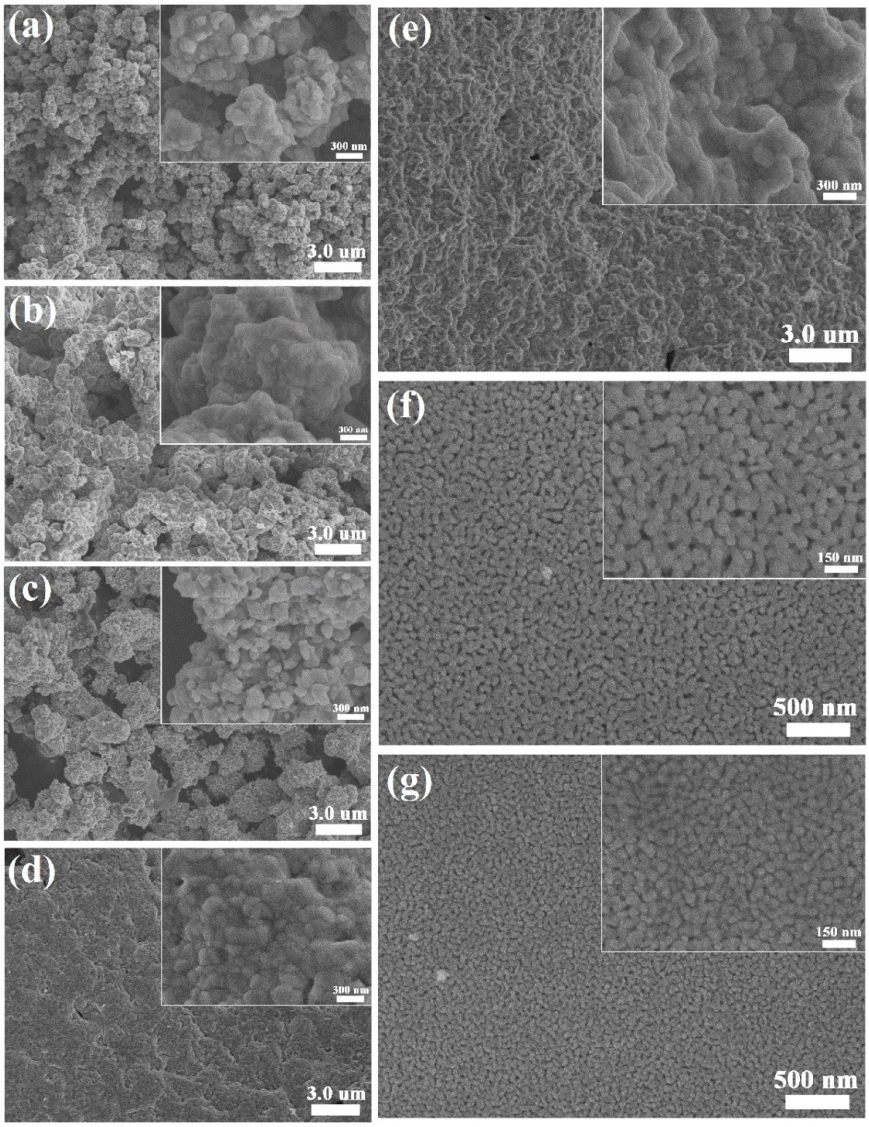

Figure S3. SEM images of $NiFe_2O_4$ nano-granules with different DMF concentration, (a) 0%, (b) 13%, (c) 33%, (d) 53%, (e) 67%, (f) 87%, and (g) 100%.

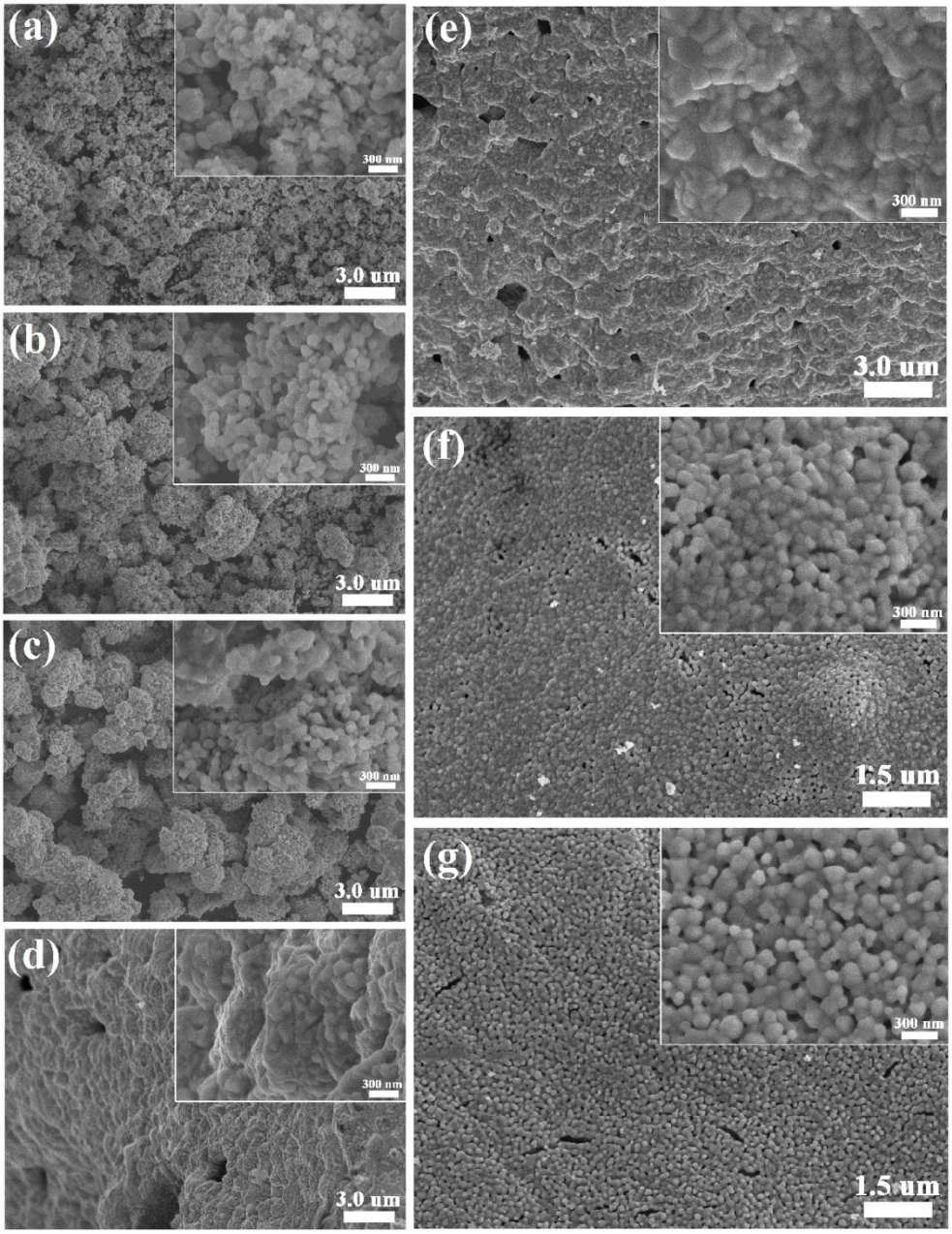

Figure S4. SEM images of $CoFe_2O_4$ nano-granules with different DMF concentration, (a) 0%, (b) 13%, (c) 33%, (d) 53%, (e) 67%, (f) 87%, and (g) 100%.

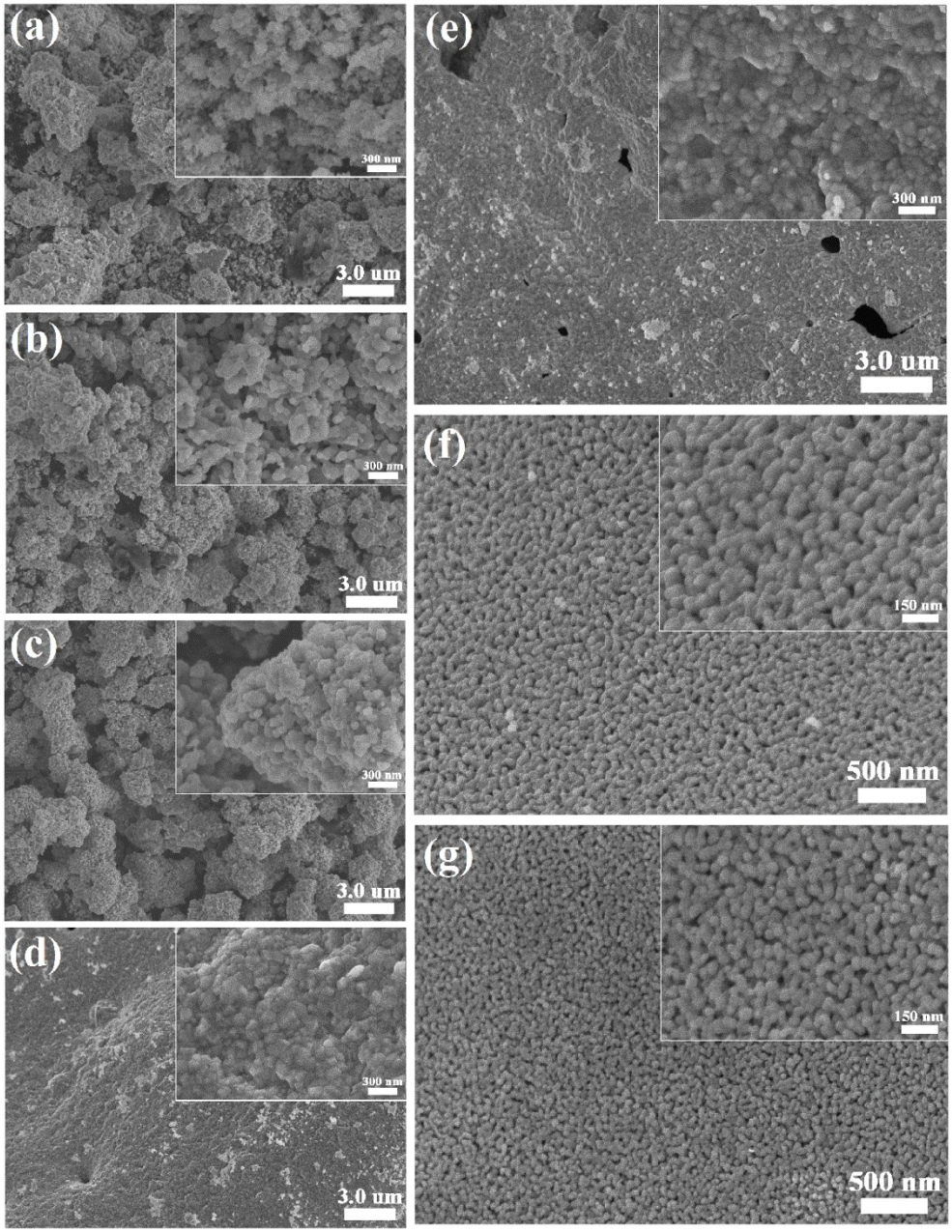

Figure S5. SEM images of $NiZnFe_2O_4$ nano-granules with different DMF concentration, (a) 0%, (b) 13%, (c) 33%, (d) 53%, (e) 67%, (f) 87%, and (g) 100%.

Typical TEM pictures of $NiFe_2O_4$, $CoFe_2O_4$, and $NiZnFe_2O_4$ nano-granules with different DMF concentration (0%, 53%, and 100%) are shown in Figure S6, S7, and S8, respectively. The results are consistent with SEM results. The morphologies of all samples also change gradually from bulk and dispersive particles to the compact and uniform nano-granules with the improvement of DMF concentration. In particular, the crystallinity of nano-granules in the pure DMF (100%) presents better when compared with low DMF samples.

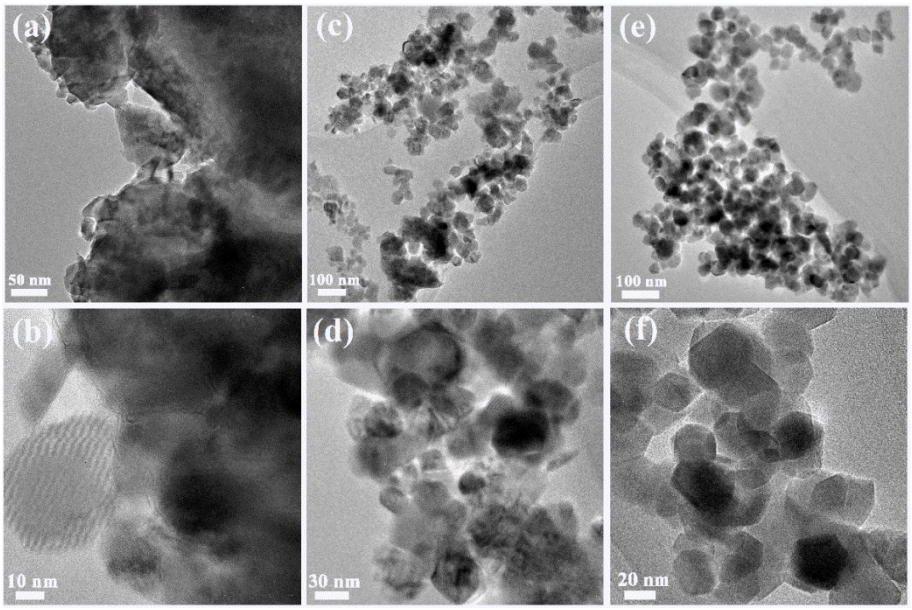

Figure S6. TEM images of $NiFe_2O_4$ nano-granules with different DMF concentration, (a-b) 0%, (c-d) 53%, and (e-f) 100%.

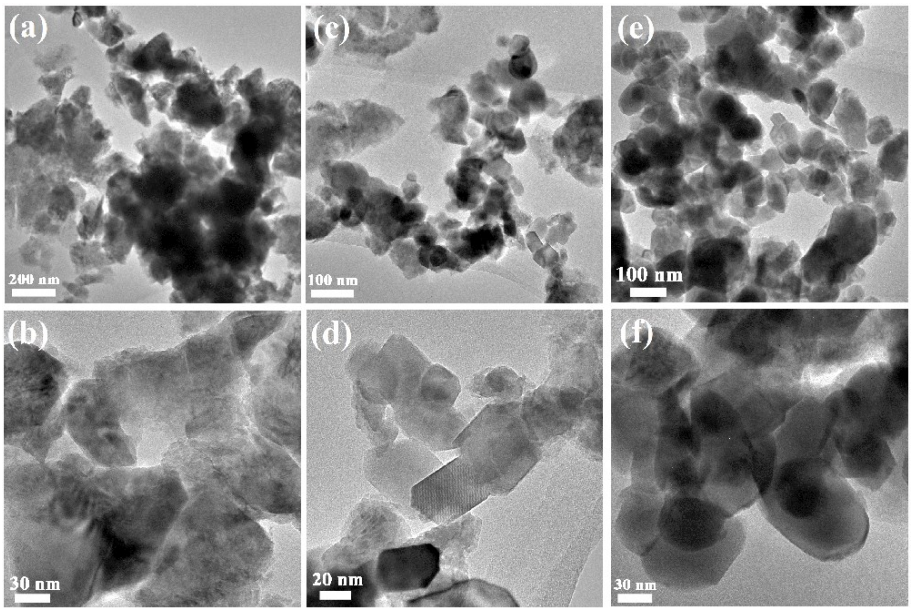

Figure S7. TEM images of $CoFe_2O_4$ nano-granules with different DMF concentration, (a-b) 0%, (c-d) 53%, and (e-f) 100%.

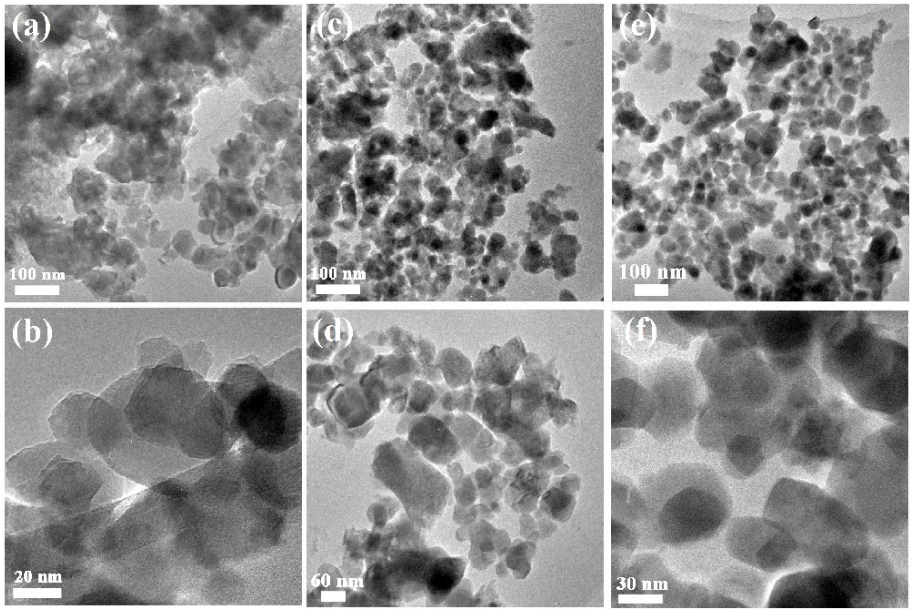

Figure S8. TEM images of $NiZnFe_2O_4$ nano-granules with different DMF concentration, (a-b) 0%, (c-d) 53%, and (e-f) 100%.

Room temperature hysteresis loop of $NiFe_2O_4$, $CoFe_2O_4$, and $NiZnFe_2O_4$ nano-granules with different DMF concentration are shown in Figure S9 (a-c), respectively. The saturation magnetization (M_s) and coercivity (H_c) obtained from the loops are also shown in Figure S9 (d-f). M_s of the $NiFe_2O_4$ nano-granules is decreased with the improvement of DMF concentration (0%~33%), and then increased directly until the DMF concentration reaching to 100%. But H_c of the nano-granules presents an opposite results when compared with M_s. H_c is enhanced firstly and then reduced with the improvement of DMF concentration. Combining the results of XRD spectra in Figure S2, we can deduce that this is due to the improvement of non-magnetic α-Fe_2O_3 phase with the increased DMF concentration (0%~33%), which leads to a relative reduction of magnetic MFe_2O_4, and the total quality of magnetic moments are dropped, thus, M_s decreases sharply. The enhanced H_c at low DMF concentration (0%~33%) is caused by the pinning of the impurity α-Fe_2O_3. However, when the DMF concentration further increases (53%~100%), the impurity α-Fe_2O_3 phase is decreased, and the crystallization of ferrite are better. M_s of nano-granules is improved, and H_c is decreased.

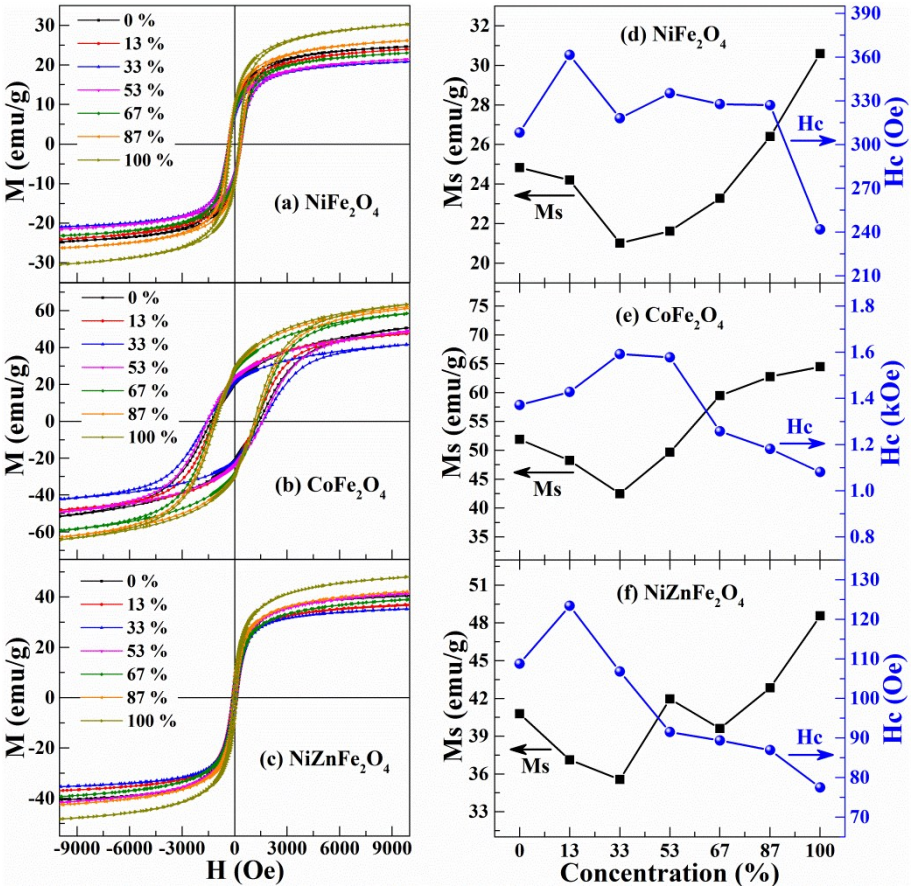

Figure S9. Room temperature hysteresis loop of $NiFe_2O_4$ (a), $CoFe_2O_4$ (b), $NiZnFe_2O_4$ (c) nano-granules with different DMF concentration. And its corresponding saturation magnetization and coercivity (d-f).

Part III

The results of obtained MFe_2O_4 nano-granules under different calcination temperatures (CT).

Figure S10 shows XRD patterns of $NiFe_2O_4$ (a) and $CoFe_2O_4$ (b) nano-granules under different CT. As shown in Figure S10 (a), it can be seen that as CT increases from 100°C to 200°C, the diffraction spectra of samples transform from no peak (100°C) to good γ-Fe_2O_3 (JCPDS#39-1346) and NiO phase (JCPDS#47-1049) (200°C). When CT increases to 300°C, γ-Fe_2O_3 is crystallized much better, and part of γ-Fe_2O_3 changes to α-Fe_2O_3 phase (JCPDS#80-2377) at the same time. While CT continues increasing to 400°C, $NiFe_2O_4$ phase can be observed. As the temperature rises to 500~600°C, the nano-granules are almost composed with α-Fe_2O_3 and $NiFe_2O_4$. The

structures of samples change from mixed phases to $NiFe_2O_4$ ferrites. Finally, when the temperature exceeds 700°C, the impurities of samples disappear, and pure $NiFe_2O_4$ nano-granules are achieved. For the $CoFe_2O_4$ nano-granules shown in Figure S10 (b), the calcination process is almost the same with that of $NiFe_2O_4$. The diffraction peaks of CoO can be well indexed according to JCPDS#48-1719. The only difference is that the crystalline temperature of $CoFe_2O_4$ is lower about 100°C than $NiFe_2O_4$ nano-granules.

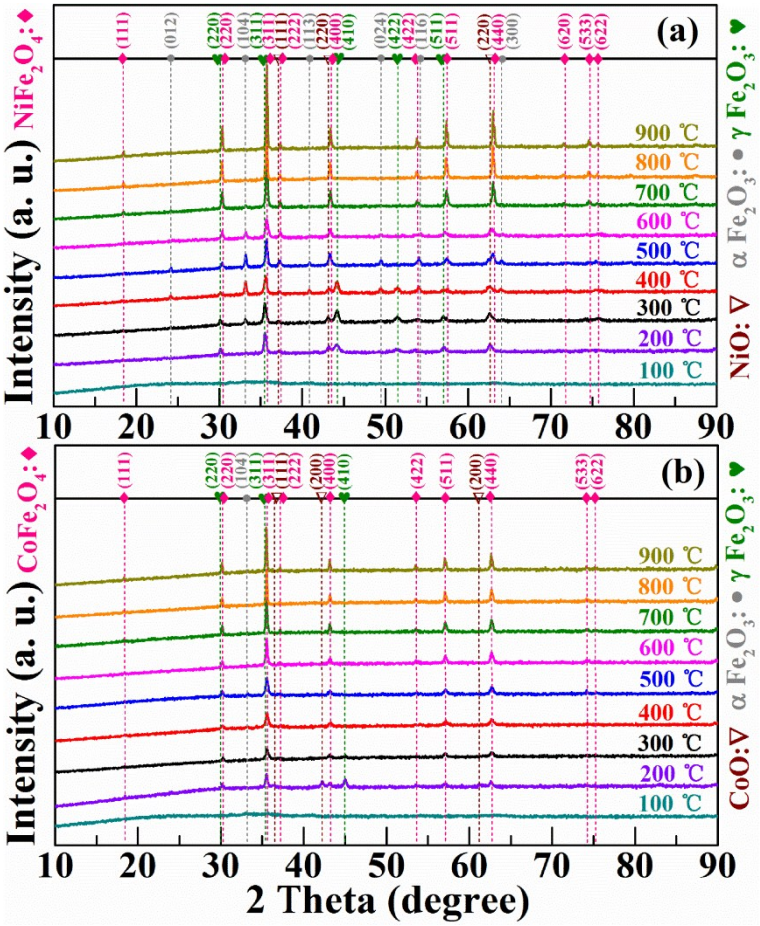

Figure S10. XRD patterns of $NiFe_2O_4$ (a) and $CoFe_2O_4$ (b) nano-granules under different CT.

Figure S11-S12 shows SEM images of $NiFe_2O_4$ and $CoFe_2O_4$ nano-granules under different CT. It can be observed that the morphologies change obviously with the improvement of CT. The results indicate various kinds of reunited and irregular particles can be seen in Figure S11 (a-b). Combining with XRD results in Figure S10 (a-b), those variety classes of littery particles may represent γ-Fe_2O_3, α-Fe_2O_3, NiO (or CoO), and $NiFe_2O_4$ (or $CoFe_2O_4$). Afterwards, the particle (Figure S11-S12 c-d) causes a change of topography in shapes, which are formed by compact and well-

regulated nano-granules. For $NiFe_2O_4$ samples, when CT is 700°C (Figure S11e), a large quantity of uniform-sized nano-granules is achieved, while $CoFe_2O_4$ nano-granules are achieved at 600°C (Figure S12d). This further confirms that the crystalline temperature of $CoFe_2O_4$ is lower than that of $NiFe_2O_4$ nano-granules. However, when CT continues increasing ($NiFe_2O_4$>700°C, $CoFe_2O_4$>600°C), the particles show an increased grain growth (Figure S11 f-g for $NiFe_2O_4$, Figure S12 e-g for $CoFe_2O_4$).

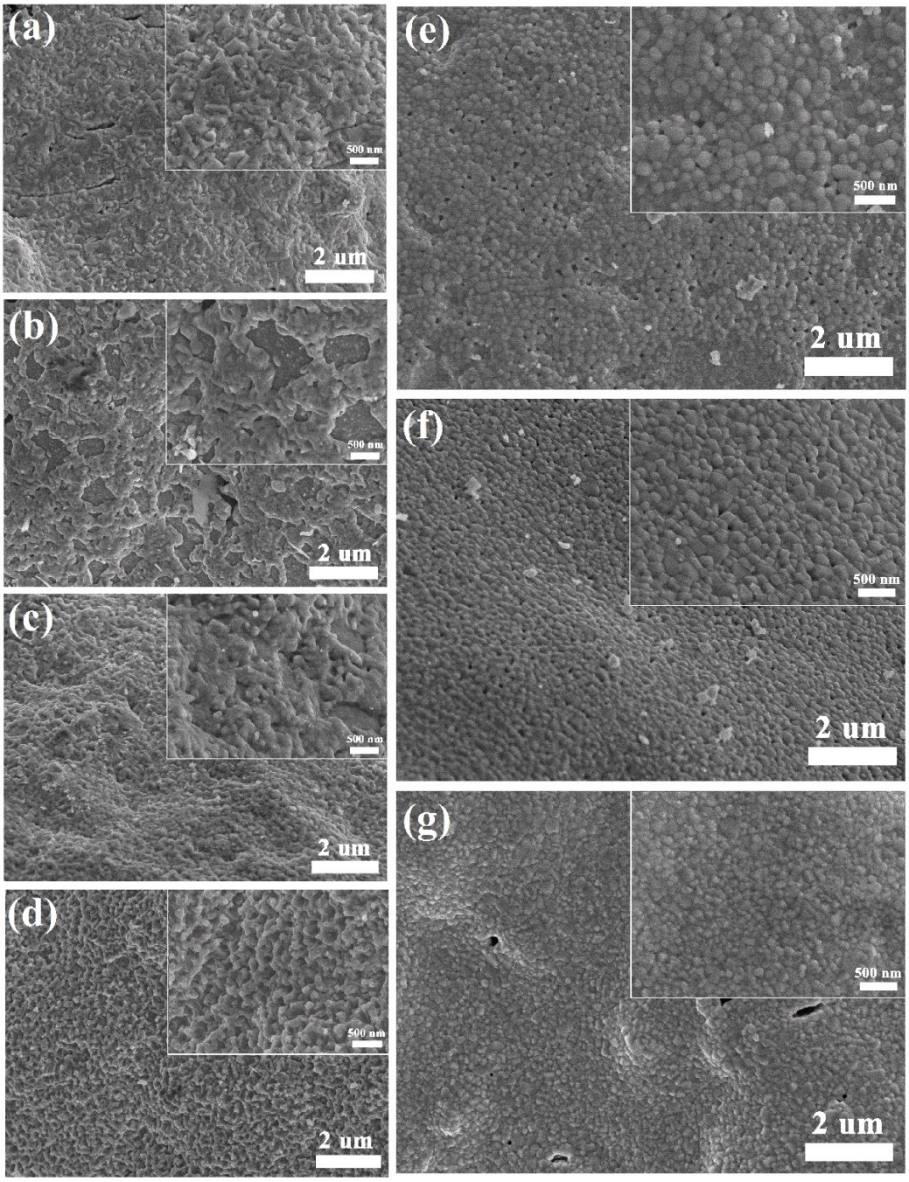

Figure S11. SEM images of $NiFe_2O_4$ nano-granules under different CT, (a) 300°C, (b) 400°C, (c) 500°C, (d) 600°C, (e) 700°C, (f) 800°C, and (g) 900°C.

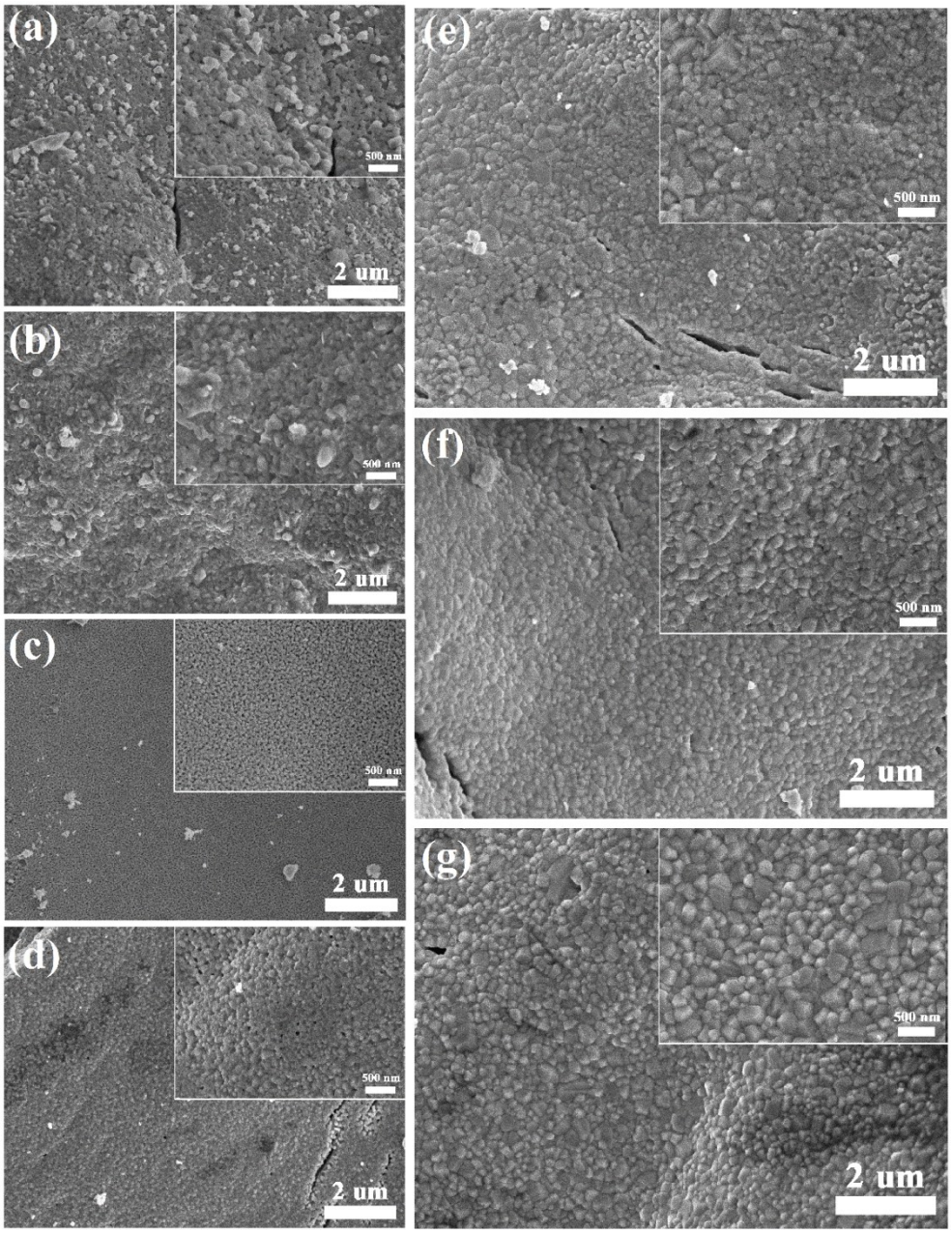

Figure S12. SEM images of $CoFe_2O_4$ nano-granules under different CT, (a) 300°C, (b) 400°C, (c) 500°C, (d) 600°C, (e) 700°C, (f) 800°C, and (g) 900°C.

Figure S13 shows room temperature hysteresis loop of $NiFe_2O_4$ (a) and $CoFe_2O_4$ (b) nano-granules under different CT, and its corresponding M_s and H_c are also shown in Figure S13 (c-d). As shown in Figure S13 (a), it can be observed that the amorphous structure (100°C) of sample displays none-magnetic properties. After the specimen is calcined at about 200°C, the loop shows perfect magnetism because of the formation of magnetite γ-Fe_2O_3. When CT increases to 300°C, thanks to the presence of none-magnetic α-Fe_2O_3, M_s of the sample at 300°C displays a little decrease. Whereafter, CT continues being increased to 400°C, γ-Fe_2O_3 is decreased, α-Fe_2O_3 is increased,

and a little $NiFe_2O_4$ is generated, M_s is further reduced because of the increased none-magnetic α-Fe_2O_3. As CT rises continuously to 500~600°C, due to the decreased α-Fe_2O_3 and the improvement of $NiFe_2O_4$ nano-granules, M_s is also enhanced immediately. Finally, when CT exceeds 700°C, there will cause an increased grain size of $NiFe_2O_4$ nano-granules from the above SEM results, and the enhanced grain size leads to the improvement of M_s. Noticeably, M_s of sample at 200°C (γ-Fe_2O_3 phase) is higher than that of 700°C ($NiFe_2O_4$ phase), this is because that M_s of pure γ-Fe_2O_3 is intrinsically larger than pure $NiFe_2O_4$. But M_s of pure $CoFe_2O_4$ is intrinsically larger than pure γ-Fe_2O_3. Moreover, the crystalline temperature of $CoFe_2O_4$ is about 100°C lower than that of $NiFe_2O_4$ nano-granules, thus, M_s of pure $CoFe_2O_4$ is improved from 600°C.

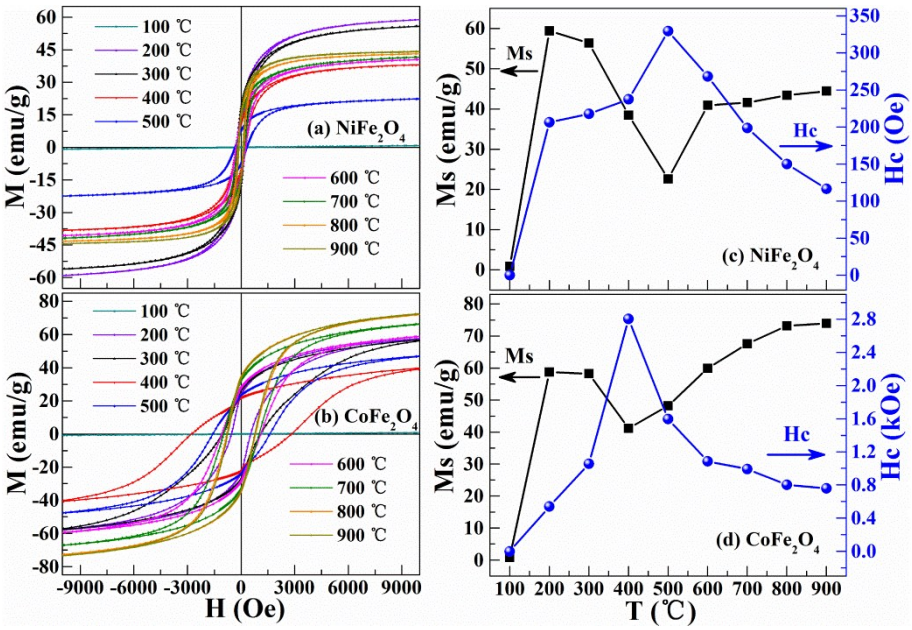

Figure S13. Room temperature hysteresis loop of $NiFe_2O_4$ (a) and $CoFe_2O_4$ (b) nano-granules under different CT. And its corresponding M_s and H_c (c-d).

Part IV

Summary of the suitable preparing parameters and synthesizing other MFe_2O_4 nano-granules.

According to the results of various DMF concentrations, MFe_2O_4 nano-granules will be achieve with perfect feature and property in pure DMF. From the results of different CT above, it demonstrates that low CT is not beneficial to the crystallization of pure MFe_2O_4 nano-granules, and it will cause the impurity phase at any of the low calcination temperature. As the general results, large quantities of uniform nano-

granules will be achieved at about 680°C in pure DMF.

Part V

The possibility of synthesizing magnetite γ-Fe_2O_3 nano-granules.

Figure S14 shows XRD patterns of all the samples with different CT. It can be seen that as CT increased from 100°C to 200°C, the diffraction spectra of samples transform from no peak (100°C) to good single γ-Fe_2O_3 phase (150°C and 200°C) with the cubic crystal system (JCPDS#39-1346), and all the diffraction peaks can be well indexed. We can determine that the obtained particles are γ-Fe_2O_3 rather than α-Fe_2O_3, due to XRD pattern of α-Fe_2O_3 (JCPDS#80-2377) being different from γ-Fe_2O_3[1,2]. However, the samples present α-Fe_2O_3 phase (JCPDS#80-2377) when CT exceeds 250°C. The emergence of impurity phase, i.e., α-Fe_2O_3, is more evident with the raised temperature (300°C ~400°C). These XRD results indicate that the oxide of iron cannot crystallize when CT is below 100°C, but α-form is observed as CT exceeds 250°C. It is well known that γ-Fe_2O_3 can be further transformed into α-Fe_2O_3 at higher temperature[3,4].

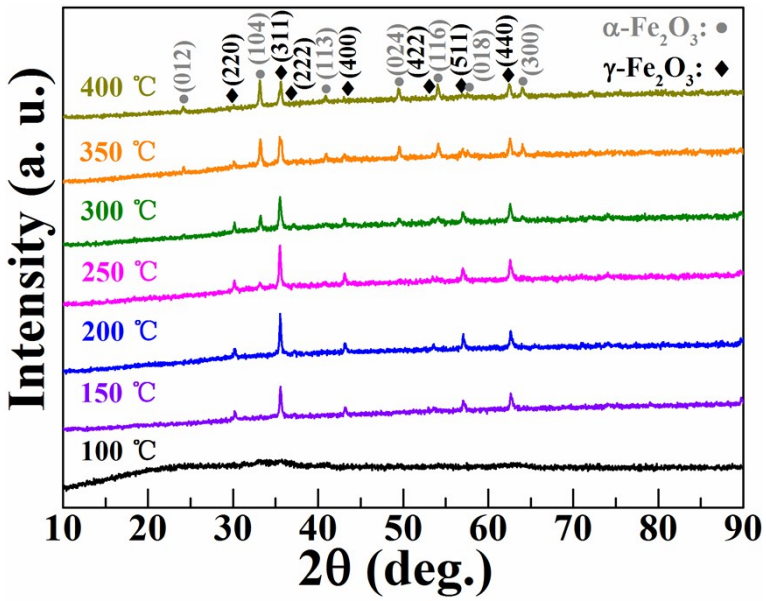

Figure S14. XRD patterns of γ-Fe_2O_3 nano-granules with different CT.

Figure S15 shows SEM images of the samples under different calcination temperature (CT). It can be observed that the morphologies change obviously with the increased CT. The results indicate the sample (100°C of Figure S15a) presents a number of bulk

particles. Afterwards, the particle (150°C of Figure S15b) causes a change of topography in shapes, and forms compact and well-regulated nano-granules. Especially, when CT is 200°C, a large quantity of uniform-sized nano-granuless is achieved. However, when CT increases continuously (250~400°C of Figure S15 d-g), the particle shows an increased grain growth (Figure S15 d-e). The particle size changes undefined, and strong pieces of reunited particles are observed with the improvement of CT (Figure S15 f-g).

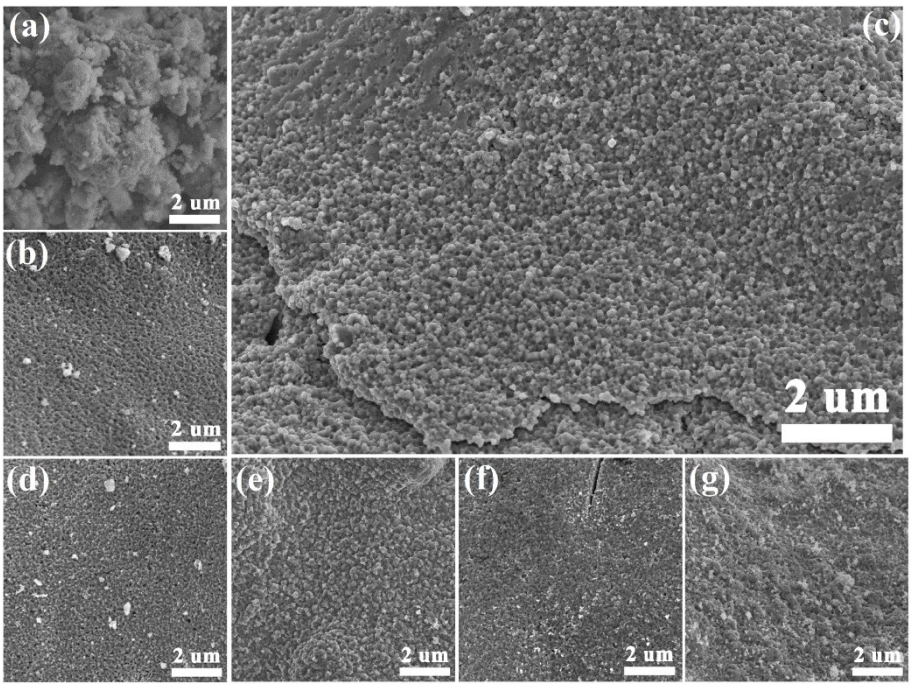

Figure S15. SEM images of of nano-granules with different CT (a) 100℃, (b) 150℃, (c) 200℃, (d) 250℃, (e) 300℃, (f) 350℃, and (g) 400℃, respectively.

In order to distinguish the chemical composition of γ-Fe_2O_3, we further conduct XPS measurement of pure γ-Fe_2O_3 nano-granules, which are displayed in Figure S16. Except for Fe 2p, O 1s and C 1s peaks appearing on their spectra, no redundant peaks appear together in the γ-Fe_2O_3 nano-granules. C element belongs to the carbon contaminants absorbed on the surface of the tested samples. In particular, Fe $2p_{3/2}$ orbit (Figure S16b) exhibits the peaks at 710.6 and 724.1 eV, which is the characteristic peak of the 3^+ ion in γ-Fe_2O_3[1,5], and there is no signal or shoulder at smaller binding energies as would be expected for the presence of the 2^+ ion (~708 eV)[6,7]. Furthermore, an additional peak at about 718.7 eV is the shakeup satellite peak, which also indicates the absence of the 2^+ ion[5,6]. XPS results further confirm the judgment of XRD spectra (Figure S15).

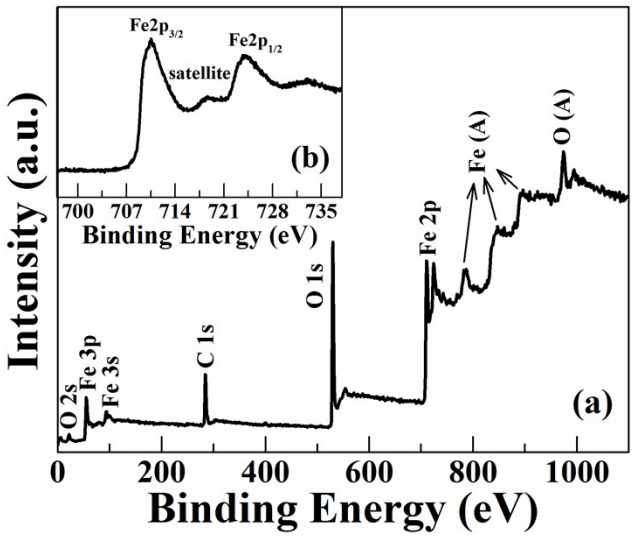

Figure S16. XPS patterns of γ-Fe_2O_3 nano-granules under 200℃; (a) Full scanned XPS spectra, (b) XPS spectra of Fe 2p core-level.

The room temperature magnetic performance of products is discussed in Figure S17. As the foreseeing, the none-crystalline sample (100°C) has no magnetism. When CT is improved to150°C, i.e. γ-Fe_2O_3 appears, the nano-granules emerge strong magnetism immediately, and M_s is about 61 emu/g. Particularly, when CT reaches to 200°C, due to the better crystallinity than that of 150°C, M_s increases to 74 emu/g, which is comparable with bulk γ-Fe_2O_3 sample[8,9], but much larger than other γ-Fe_2O_3 nano-granules[3,10-12]. However, when CT exceeds 250°C, M_s decreases. This is because the presence of non-magnetic α-Fe_2O_3, which leads to the relative reduction of magnetic γ-Fe_2O_3, and the magnetic moment total quality drops. With increased CT (250~400°C), the impurity α-Fe_2O_3 phase appears more obviously (which can be confirmed by XRD results in Figure S14), thus, M_s is reduced gradually.

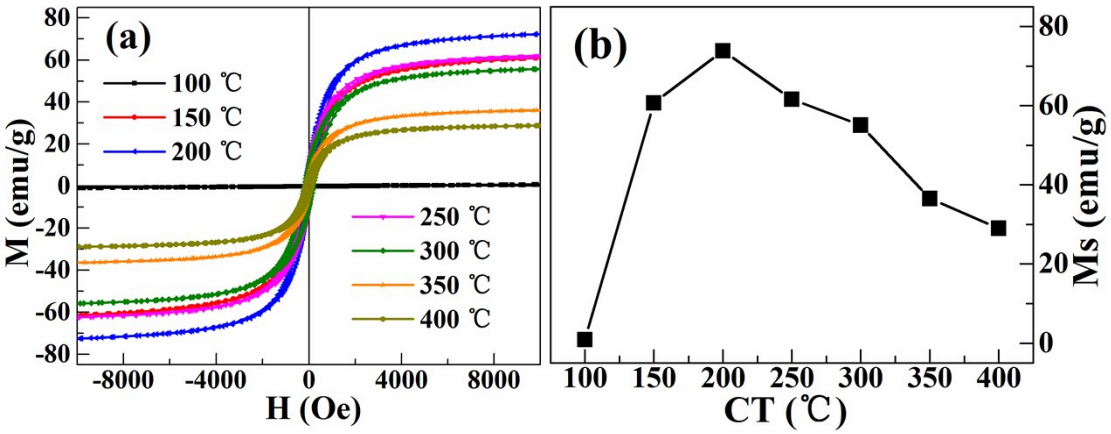

Figure S17. (a-b) Room temperature *M-H* loops for γ-Fe_2O_3 nano-granules and its

corresponding M_s under different CT.

Part VI

The possibility of preparing MFe_2O_4 nano-granules doped with nonmetal elements.

Figure S18 shows XRD patterns of all the samples with different S concentration. It can be seen that as S concentration increases from 0 mol/L to 0.3 mol/L, the samples are good single $CoFe_2O_4$ phase with the cubic crystal system and all the diffraction peaks can be well indexed. When S concentration continues increasing, the emergence of impurity phase α-Fe_2O_3 is evident at higher S content (0.5 mol/L). Moreover, the diffraction (311) peaks of the samples (0 mol/L~0.3 mol/L) shift a little to lower angles as S concentration increases due to the lattice expansion, and the lattice of $CoFe_2O_4$ expands with the increasement of S element. The results indicate that S element is effectively incorporated into the $CoFe_2O_4$ nano-granules.

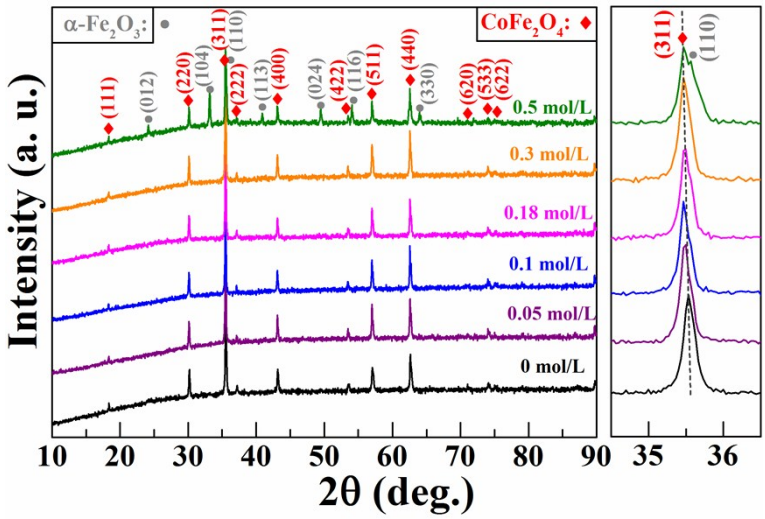

Figure S18. XRD patterns of all the samples with different S concentration.

Figure S19 shows typical SEM images of the samples with different S concentration. It can be observed that the morphologies and the particle sizes change obviously after S element doping. The pure $CoFe_2O_4$ and S-doped $CoFe_2O_4$ nano-granules shown in Figure S19 (a-b) are composed of a large quantity of flat and uniform microspheres with average sizes about 90~100 nm. In addition, the doping effect of S element to $CoFe_2O_4$ nano-granules causes an increased grain growth and agglomeration as shown in the Figure S19 (b). Afterwards, as S content continues increasing (Figure S19 c-e), the micrographs of pure and S-doped $CoFe_2O_4$ nano-granules reveal the shape and arrangement modification are changed from the compact granules to sparse but reunited coral-like structure, especially when S concentration is 0.3 mol/L. When S

concentration increases to 0.5 mol/L, the morphology of the sample becomes more disarray, and reunites bulk with nano-granules on them.

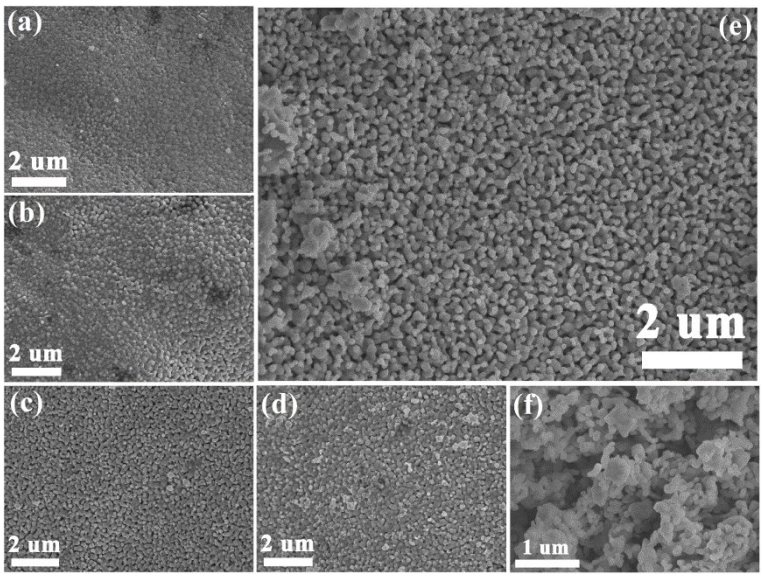

Figure S19. SEM imagines of obtained $CoFe_2O_4$ samples doped with different S contents: (a) 0mol/L, (b) 0.05mol/L, (c) 0.1 mol/L, (d) 0.18 mol/L, (e) 0.3 mol/L, and (f) 0.5 mol/L, respectively.

As a representative, the chemical elemental composition of S-doped $CoFe_2O_4$ with S concentration of 0.3 mol/L is further characterized by TEM. In Figure S20 (a), TEM image clearly reveals that a lot of well-shaped coral-like morphology. TEM imagine shown in Figure S20 (a) is consistent with SEM images presented in Figure S19 (b). Figure S20 (b) shows a typical HAADF-STEM image of $CoFe_2O_4$ with S concentration of 0.3 mol/L. It directly certifies the curving-strip-particles morphology again. S distribution was studied by STEM mapping. As shown in Figure 21 (c), (d), (e) and (f), all the composition of Fe, Co, O and S elements are evenly distributed uniformly throughout the $CoFe_2O_4$ coral-like nanoparticles, which confirms that S has been efficiently incorporated into $CoFe_2O_4$ nanoparticles.

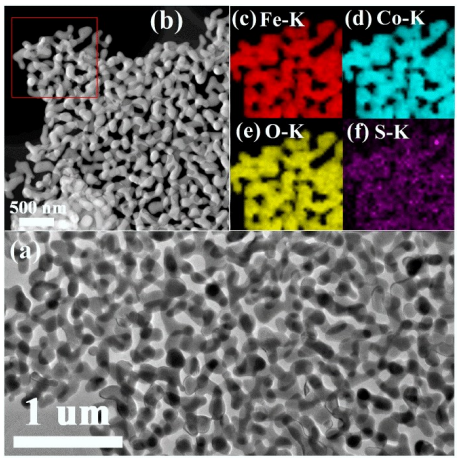

Figure S20. Morphology of $CoFe_2O_4$ sample obtained with S concentration of 0.3 mol/L: (a) a representative TEM image; (b) HAADF-STEM image; Elemental mappings of the particles of (c) iron element; (d) cobalt element; (e) oxygen element and (f) sulfur element.

The composition and S moieties are examined by XPS, which are displayed in Figure S21. Figure S21 (a) shows the full scanned XPS spectra of the $CoFe_2O_4$ samples doped with S element (0.3 mol/L) and none element S (0 mol/L). Except for the corresponding element, Co 2p, Fe 2p, O 1s and C 1s peaks appear in the pure $CoFe_2O_4$ and S-doped $CoFe_2O_4$, S 2s and S 2p peaks also appear together in S-doped $CoFe_2O_4$ coral-like nano-granules. C element belongs to the carbon contaminants absorbed on the surface of the tested samples. Figure S21 (b) exhibits the amplifying full scan in small binding energy, in which S 2s and S 2p peaks could be observed obviously. Figure S21 (c) presents S 2p core-level XPS spectra of two samples recorded in the high-resolution mode. It can be seen that S-doped sample exhibits obvious S peak, whereas that of the sample without S doesn't show S peak. According to XPS data, we further prove that S element has been incorporated in $CoFe_2O_4$ nano-granules.

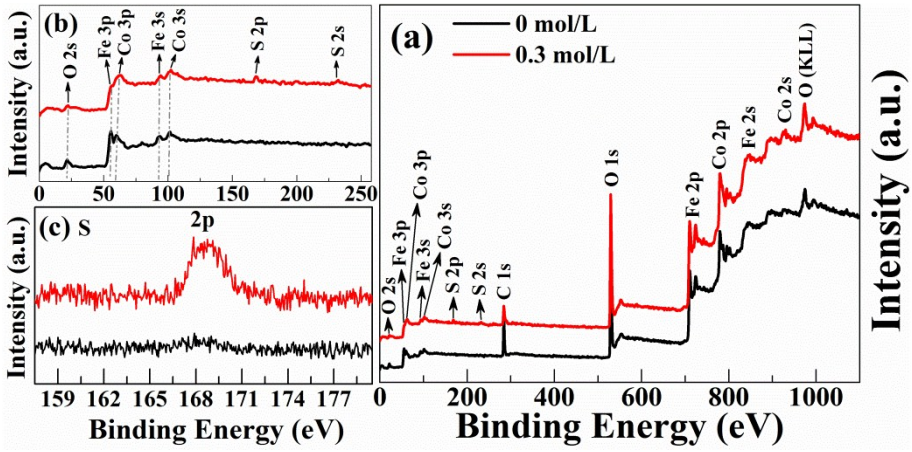

Figure S21. XPS of the pure $CoFe_2O_4$ (0 mol/L) and $CoFe_2O_4$ samples doped with S (0.3mol/L): (a) the full scan, (b) the amplifying full scan in small binding energy, and (c) S 2p level.

The room temperature magnetic performance of products is discussed in Figure S22 (a). For the pure $CoFe_2O_4$ without S doping, M_s is about 67 emu/g, which is close to the theoretical values of 71.2 emu/g[13]. Figure S22 (b) exhibits S concentration dependence of M_s of all samples. M_s of all S-doped $CoFe_2O_4$ nanoparticles is above 67 emu/g and it monotonically increases with S concentration changed from 0.05 mol/L to 0.3 mol/L. Particularly, when S concentration reaches 0.3 mol/L, M_s increases to 81 emu/g, which is much larger than other $CoFe_2O_4$ nanoparticles [13-20]. Significantly, S-doped $CoFe_2O_4$ nanoparticles in this work are quite different from the former metal-doped $CoFe_2O_4$ nanoparticles. M_s of former $CoFe_2O_4$ nanoparticles mainly decrease after doping with metal, while M_s is improved greatly in this work.

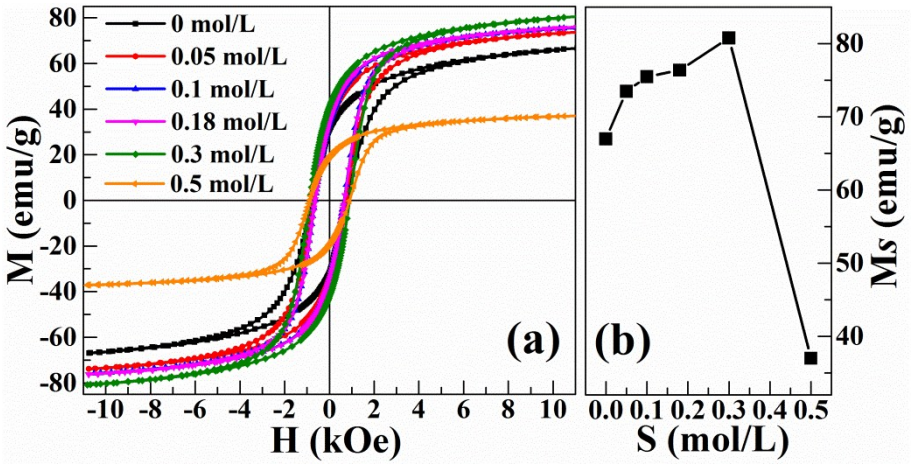

Figure S22. (a) *M-H* loops for pure $CoFe_2O_4$ nano-granules (S: 0mol/L) and S-doped $CoFe_2O_4$ nano-granules with different S concentration; (b) S concentration dependence of M_s for the corresponding samples.

Figure S23 shows XRD patterns of all the samples with different C concentration. The results are nearly the same as C-doped $CoFe_2O_4$, but there is no impure phase at any C content. The expanded lattice with the increasing of C element also indicates that the C element is effectively incorporated into the $CoFe_2O_4$ nano-granules.

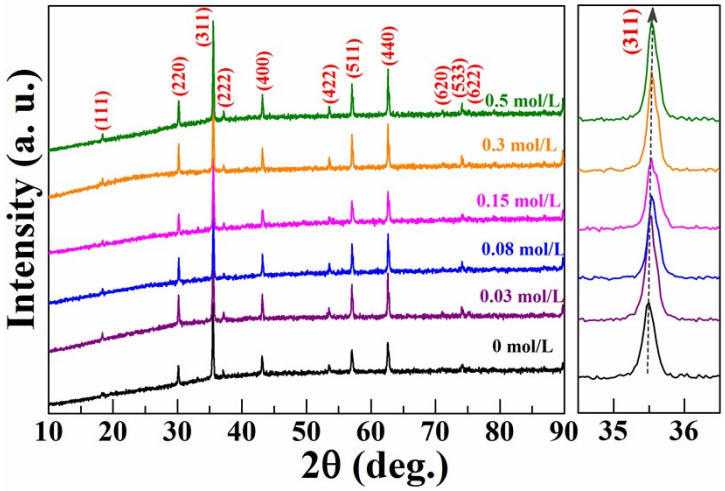

Figure S23. XRD patterns of all the samples with different C concentration.

Figure S24 shows typical SEM images of the samples with different C concentration. It can be observed that the morphologies and the particle sizes change obviously after C element doping. The pure $CoFe_2O_4$ and C-doped $CoFe_2O_4$ nano-granules in Figure S24 (a-b) are composed of a large quantity of flat and uniform microspheres which is no different with C-doped $CoFe_2O_4$. Afterwards, as C content continues increasing (Figure S24 c-f), comparison of the micrographs of pure and C-doped $CoFe_2O_4$ nano-granules, reveals the grains size is increased and the shape changes from the compact granules to square with the improvement of C concentration, especially when C concentration is 0.5 mol/L.

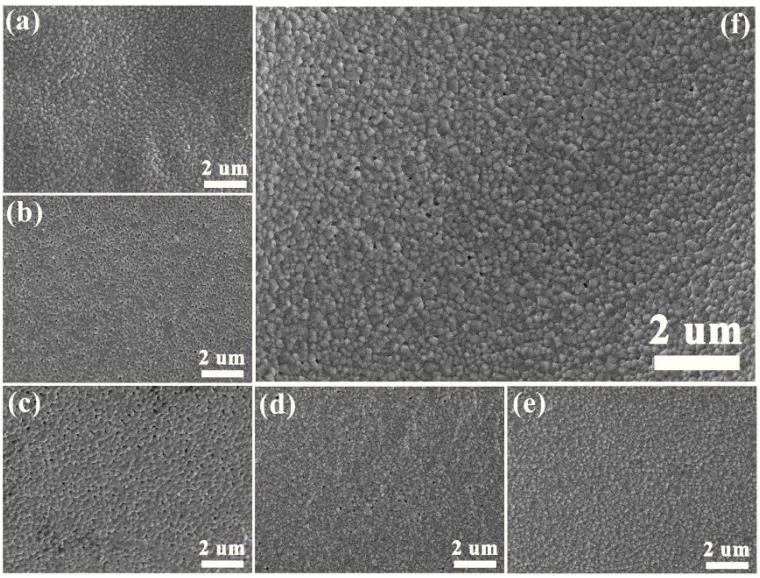

Figure S24. SEM imagines of obtained $CoFe_2O_4$ samples doped with different C contents: (a) 0 mol/L, (b) 0.03mol/L, (c) 0.08 mol/L, (d) 0.15 mol/L, (e) 0.3 mol/L, and (f) 0.5 mol/L, respectively.

The composition and C moieties are examined by XPS, which is displayed in Figure S25. Figure S25 (a) shows the full scanned XPS spectra of the $CoFe_2O_4$ samples doped with C element (0.5 mol/L) and none element C (0 mol/L). Co 2p, Fe 2p, O 1s and C 1s peaks appear in the pure $CoFe_2O_4$ and C-doped $CoFe_2O_4$, but the intensity of C 1s seems a little higher than pure $CoFe_2O_4$. Figure S25 (b) presents C 1s core-level XPS spectra of two samples recorded in the high-resolution mode. C element of pure $CoFe_2O_4$ (0 mol/L) belongs to the carbon contaminants absorbed on the surface of the tested samples. However, it can be seen that C-doped sample exhibits two obvious peaks, the peak at 248.6 belongs to position of C-C/C=C, while the peak at about 288.7 is the position of C=O. According to XPS data, we further prove that C element has been incorporated in $CoFe_2O_4$ nano-granules.

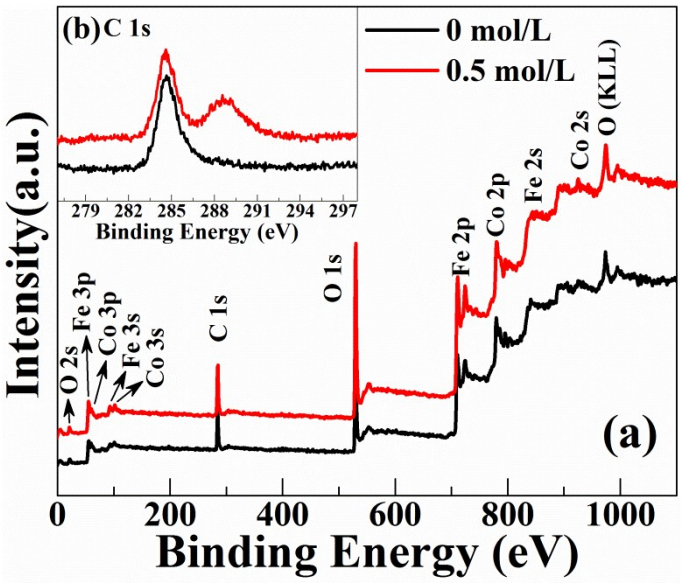

Figure S25. XPS of the pure $CoFe_2O_4$ (0 mol/L) and $CoFe_2O_4$ samples doped with C (0.5 mol/L): (a) the full scan, and (b) C 1s level.

The room temperature magnetic performance of products is discussed in Figure S26. M_s of all C-doped $CoFe_2O_4$ nanoparticles are above 67 emu/g and it monotonically increases with the increased C concentration changing from 0 mol/L to 0.5 mol/L. M_s increases to 81 emu/g, when C concentration reaches 0.5 mol/L, which is much larger than other $CoFe_2O_4$ nanoparticles, the results is the same with S-doped $CoFe_2O_4$ nanoparticles.

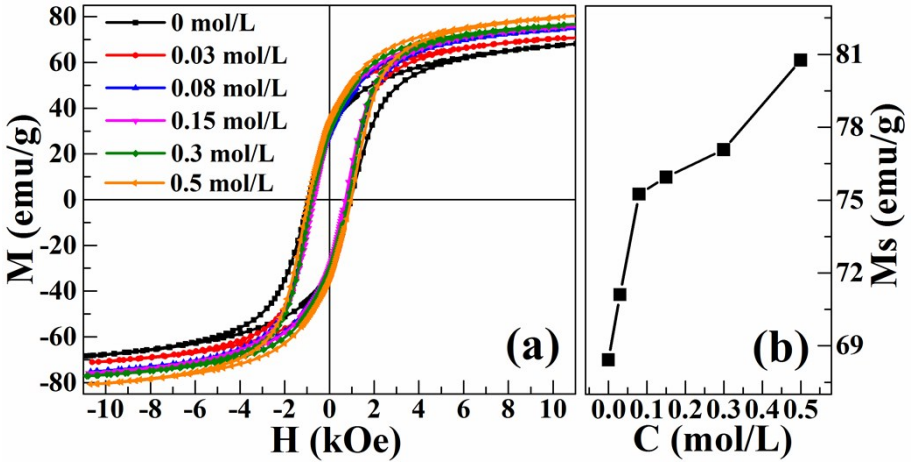

Figure S26. (a) *M-H* loops for pure $CoFe_2O_4$ nano-granules (C: 0 mol/L) and C-doped $CoFe_2O_4$ nano-granules with different C concentration; (b) C concentration dependence of M_s for the corresponding samples.

Reference

1 Zhang, Y. *et al.* Two-in-One Strategy for Effective Enrichment of Phosphopeptides Using Magnetic Mesoporous γ-Fe_2O_3 Nanocrystal Clusters. *ACS Appl. Mater. Interfaces* **5**, 614-621 (2013).

2 Zhong, L. S. *et al.* Self‐Assembled 3D flowerlike iron oxide nanostructures and their application in water treatment. *Adv. Mater.* **18**, 2426-2431 (2006).

3 Lai, J. *et al.* Doping γ-Fe_2O_3 Nanoparticles with Mn(III) Suppresses the Transition to the α-Fe2O3 Structure. *J. Am. Chem. Soc.* **125**, 11470-11471 (2003).

4 Yen, F. S., Chen, W. C., Yang, J. M. & Hong, C. T. Crystallite Size Variations of Nanosized Fe_2O_3 Powders during γ- to α-Phase Transformation. *Nano Lett.* **2**, 245-252 (2002).

5 Rao, P. M. & Zheng, X. Unique Magnetic Properties of Single Crystal γ-Fe_2O_3 Nanowires Synthesized by Flame Vapor Deposition. *Nano Lett.* **11**, 2390-2395 (2011).

6 Fujii, T. *et al.* In situ XPS analysis of various iron oxide films grown by NO2-assisted molecular-beam epitaxy. *Phys. Rev. B* **59**, 3195-3202 (2001).

7 Gao, Y. & Chambers, S. A. Heteroepitaxial growth of alpha-Fe_2O_3, gamma-Fe_2O_3 and Fe_3O_4 thin films by oxygen-plasma-assisted molecular beam epitaxy. *J. Cryst. Growth* **174**, 446-454 (1997).

8 Wang, J., Ma, Y. & Watanabe, K. Magnetic-Field-Induced Synthesis of Magnetic γ-Fe_2O_3 Nanotubes. *Chem. Mater.* **20**, 20-22 (2008).

9 Shafi, K. V. P. M. *et al.* Magnetic Enhancement of γ-Fe_2O_3 Nanoparticles by Sonochemical Coating. *Chem. Mater.* **14**, 1778-1787 (2002).

10 Park, K. *et al.* Structural and Magnetic Properties of Gold and Silica Doubly Coated γ-Fe_2O_3 Nanoparticles. *J. Phys. Chem. C* **111**, 18512-18519 (2007).

11 Ianos, R., Taculescu, E.-A., Pacurariu, C. & Niznansky, D. gamma-Fe_2O_3 nanoparticles prepared by combustion synthesis, followed by chemical oxidation of residual carbon with H2O2. *Mater. Chem. Phys.* **148**, 705-711 (2014).

12 Lu, J., Jiao, X., Chen, D. & Li, W. Solvothermal Synthesis and Characterization of Fe_3O_4 and γ-Fe_2O_3 Nanoplates. *J. Phys. Chem. C* **113**, 4012-4017 (2009).

13 Bao, N., Shen, L., Wang, Y., Padhan, P. & Gupta, A. A Facile Thermolysis Route to Monodisperse Ferrite Nanocrystals. *J. Am. Chem. Soc.* **129**, 12374-12375 (2007).

14 Cojocariu, A. M., Soroceanu, M., Hrib, L., Nica, V. & Caltun, O. F. Microstructure and magnetic properties of substituted (Cr, Mn) - cobalt ferrite nanoparticles. *Mater. Chem. Phys.* **135**, 728-732 (2012).

15 Nongjai, R., Khan, S., Asokan, K., Ahmed, H. & Khan, I. Magnetic and electrical properties of In doped cobalt ferrite nanoparticles. *J. Appl. Phys.* **112**, 084321 (2012).

16 Prathapani, S., Vinitha, M., Jayaraman, T. V. & Das, D. Effect of Er doping on the structural and magnetic properties of cobalt-ferrite. *J. Appl. Phys.* **115**, 17A502 (2014).

17 Amiri, S. & Shokrollahi, H. Magnetic and structural properties of RE doped Co-ferrite (RE=Nd, Eu, and Gd) nano-particles synthesized by co-precipitation. *J. Magn. Magn. Mater.* **345**, 18-23 (2013).

18 Karimi, Z. *et al.* Magnetic and structural properties of nano sized Dy-doped cobalt ferrite synthesized by co-precipitation. *J. Magn. Magn. Mater.* **361**, 150-156 (2014).

19 Naik, S. R. & Salker, A. V. Change in the magnetostructural properties of rare earth doped cobalt ferrites relative to the magnetic anisotropy. *J. Mater. Chem.* **22**, 2740-2750 (2012).

20 Patange, S. M., Shirsath, S. E., Toksha, B. G., Jadhav, S. S. & Jadhav, K. M. Electrical and magnetic properties of Cr^{3+} substituted nanocrystalline nickel ferrite. *J. Appl. Phys.* **106**, 023914 (2009).